nature physics

Article

https://doi.org/10.1038/s41567-024-02539-4

A superconducting dual-rail cavity qubit with erasure-detected logical measurements

Received: 28 September 2023

Accepted: 13 May 2024

Published online: 02 July 2024

Check for updates

Kevin S. Chou[1] ✉, Tali Shemma[1], Heather McCarrick[1], Tzu-Chiao Chien[1], James D. Teoh[2,3], Patrick Winkel[2,3], Amos Anderson[1], Jonathan Chen[1], Jacob C. Curtis[2,3], Stijn J. de Graaf[2,3], John W. O. Garmon[2,3], Benjamin Gudlewski[1], William D. Kalfus[2,3], Trevor Keen[1], Nishaad Khedkar[1], Chan U. Lei[1], Gangqiang Liu[1], Pinlei Lu[1], Yao Lu[2,3], Aniket Maiti[2,3], Luke Mastalli-Kelly[1], Nitish Mehta[1], Shantanu O. Mundhada[1], Anirudh Narla[1], Taewan Noh[1], Takahiro Tsunoda[2,3], Sophia H. Xue[2,3], Joseph O. Yuan[1], Luigi Frunzio[2,3], José Aumentado[1,4], Shruti Puri[2,3], Steven M. Girvin[2,3], S. Harvey Moseley Jr.[1] & Robert J. Schoelkopf[1,2,3] ✉

A critical challenge in developing scalable quantum systems is correcting the accumulation of errors while performing operations and measurements. It is known that systems where dominant errors can be detected and converted into erasures have relaxed requirements for quantum error correction. Recently, it has been proposed that this can be achieved using a dual-rail encoding of quantum information in the microwave photon states of two superconducting cavities. One necessary step to realize this erasure qubit is to demonstrate a measurement and to flag errors as erasures. In this work, we demonstrate a projective logical measurement of a dual-rail cavity qubit with integrated erasure detection and measure the qubit idling errors. We measure the logical state preparation and measurement errors at the 0.01% level and detect over 99% of the cavity decay events as erasures. We use the precision of this measurement protocol to distinguish different types of error in this system, finding that although decay errors occur with a probability of approximately 0.2% per microsecond, phase errors occur 6 times less frequently and bit flips occur at least 150 times less frequently. These findings represent a confirmation of the expected error hierarchy necessary to concatenate dual-rail cavity qubits into a highly efficient erasure code.

Practical quantum error correction requires achieving error rates well below the threshold in physical qubits during all operations. Most platforms still require substantial improvements in fidelity of not just the gates but all operations, including state preparation and measurement (SPAM). In addition to the quest for better physical qubits with lower error rates and fewer error channels, various avenues are being investigated to address these challenges. One approach is to implement error correction using qudits or multilevel bosonic modes to provide the necessary redundancy within a single physical element[1–5], and is the only architecture to have achieved breakeven for the lifetime of a logical qubit[6–9]. Further, error correction thresholds can be less demanding if one can tailor codes[10–14] to exploit a natural or engineered noise bias in the qubits[15–19]. While on the path to error correction, there are benefits in detecting errors as they occur in physical qubits through the use of additional flag qubits dedicated to error detection[20–24].

A relatively new approach[25] is to directly build, into the physical qubit, a capability to appropriately detect[26–29] the dominant errors, thereby converting them into erasures, which are defined as detected

A full list of affiliations appears at the end of the paper. ✉e-mail: chou@quantumcircuits.com; robert.schoelkopf@yale.edu

https://doi.org/10.1038/s41567-024-02539-4

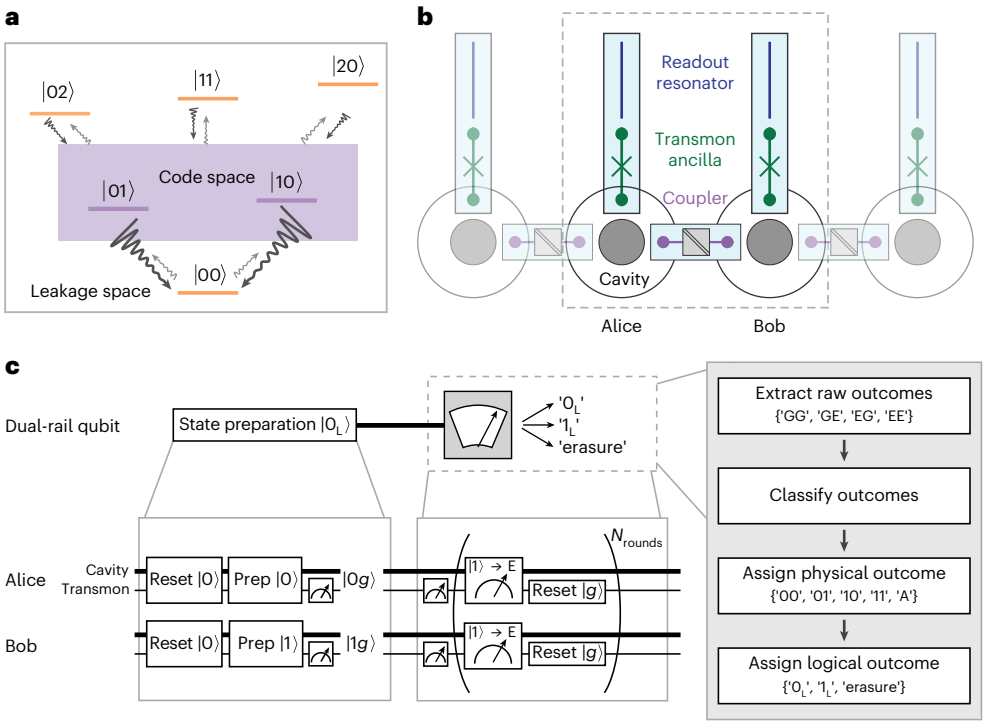

Fig. 1 | Dual-rail cavity qubit concept, implementation and measurement. **a**, The dual-rail codespace spans the states $\{|0_L\rangle, |1_L\rangle\} = \{|01\rangle, |10\rangle\}$ defined by a photon in Alice or Bob, respectively. Transitions out of the code space induced by either relaxation or heating events bring the system into a leakage space that can be detected with an appropriate measurement protocol. **b**, The dual-rail cavity qubit is implemented in a superconducting cQED module consisting of several physical modes: two three-dimensional $\lambda/4$ coaxial cavities (grey), each dispersively coupled to a transmon (green), and a resonator (blue) for control and readout. Single-qubit operations are engineered by beamsplitter interactions[38,44,45] enabled by a nonlinear coupler, constructed here as an array of three SNAIL elements operated at the zero-bias sweet spot (Supplementary Section II). There are adjacent cavity systems within this module that are not used in this experiment, shown as the shaded elements. **c**, Protocol for a logical SPAM experiment. The dual-rail logical measurement incorporates erasure detection, leading to a measurement with three outcomes: logical outcomes 0_L and 1_L and erasures. There are several steps required to decode the logical measurement, starting with the assignment of transmon outcomes, classification and assignment to one of the physical cavity outcomes ('00', '01', '10' or '11') or to an ambiguous outcome ('A') in the case of multiple rounds of measurements disagreeing, before finally assigning the logical outcome.

errors that occur at a specific time and location in the physical qubits[30]. The use of such so-called erasure qubits extends error detection to full error correction when incorporated in a higher-level stabilizer code. An erasure-qubit-based stabilizer code has a distinct advantage, as it is known that any stabilizer code can correct for twice as many erasure errors compared with Pauli errors[30]. Additionally, large-scale error correction codes benefit from a higher threshold for erasure errors[25,31,32].

A simple way to realize an erasure qubit is with dual-rail encoding, defined by the code words $|0_L\rangle = |01\rangle$ and $|1_L\rangle = |10\rangle$ (Fig. 1a). The encoding of this qubit in two spatial modes[33] or polarizations of an optical photon[34] is a well-known concept[35] that has been widely explored in linear optics platforms, and remains an active area of research[36]. The recently proposed circuit quantum electrodynamics (cQED) implementation of the dual-rail cavity qubit[37] has the distinct advantage of strong and controllable nonlinearity via a dispersively coupled transmon ancilla, which enables on-demand arbitrary state preparation, entangling gates and measurements enabled by efficient single-photon detection. Other approaches to encode and operate a qubit using a pair of superconducting microwave modes have been proposed and experimentally demonstrated[38–40]. More recently, the idea of building erasure qubits out of transmon qubits themselves has also been proposed[26]. By using superconducting microwave cavities to encode the dual-rail qubit, the cQED cavity realization is designed to leverage the high noise bias where dephasing errors are far rarer than photon loss errors[41], a property that is highly desirable for any erasure qubit. Additionally, this noise bias can be preserved during all the operations[37] and offers the prospect of converting not only the cavity photon loss but also dominant ancilla errors[41–43], into detectable erasures. Crucially, this can be achieved for a full set of single-qubit[44,45] and two-qubit gates[46], as well as for SPAM. A key design principle of the dual-rail cavity qubit is to engineer a system that exhibits a strong hierarchy of errors, with the majority of errors detectable as erasures and with the residual Pauli and leakage error rates that are orders of magnitude smaller. This hierarchy results in a qubit optimized for integration into a higher-level error correction code. Already, recent work has demonstrated single-qubit operation fidelities for a dual-rail cavity qubit in excess of 99.95% (refs. 44,45). However, to fully exploit the benefits of this encoding, several other aspects are required.

In this work, we implement logical SPAM in a dual-rail cavity qubit. We design our logical measurement to have built-in erasure detection, rendering it insensitive to any single occurrence of the dominant hardware errors, including those arising from decoherence, initialization and readout. The type of logical measurement we show is an example of end-of-the-line erasure detection, which finds use when measuring qubits at the end of an algorithm or when measuring error syndromes in a stabilizer circuit. This is in contrast with mid-circuit erasure detection, which preserves the logical information within the code space when an erasure is not detected[25]. Such a mid-circuit measurement is necessary for erasure conversion or correction and has been theoretically proposed for the bosonic cQED platform[37,46] and experimentally demonstrated in various platforms, including the use of neutral atom[28,29], transmon-based dual-rail qubits[47] and cavity-based dual-rail qubits[48].

With our end-of-the-line measurement, we obtain SPAM errors that are among the lowest for any physical qubit platform, with logical

https://doi.org/10.1038/s41567-024-02539-4

errors at the 0.01% level. Additionally, we show that over 99% of decay errors can be detected as end-of-the-line erasures. We use this logical measurement to probe idling bit-flip and dephasing error rates in a dual-rail qubit, finding that they are smaller than the measured erasure rates. Specifically, for this system, we measure a cavity decay rate of ~0.2% per microsecond, with phase and bit-flip errors measured to be a factor of 6 times and at least 150 times less likely, respectively. The development of a logical measurement with precise erasure detection is a key step for the dual-rail cavity qubit approach and enables a detailed characterization of both erasures and underlying small errors.

Results

Characterizing dual-rail SPAM

We first describe the principle of measurement for the dual-rail cavity qubit. The logical measurement of a dual-rail cavity qubit detects which cavity, if any, contains the photon. In contrast to conventional qubit measurements, where performance is limited by misassignment and transition errors during readout[49,50], the logical measurement has the additional capability of labelling most of these readout errors as well as cavity leakage errors as erasures. The logical measurement is expected to have both low logical misassignment errors and be a highly sensitive detector of leakage due to decay errors (photon loss), as well as ideally incurring only a small penalty from additional erasures due to readout errors. These properties are essential for a good dual-rail cavity qubit.

In our hardware implementation, each cavity has an individual ancilla transmon and readout for control and measurement (Fig. 1b) and allows the simultaneous measurement of both cavities. We use a nonlinear coupler (Supplementary Section II) to enable a parametric interaction between the cavities. We implement beamsplitter-type interactions for logical single-qubit gates and quantify gate errors to be less than 10^{-3} (Supplementary Section III).

We describe our protocols for SPAM in the dual-rail encoding (Supplementary Section V provides more details). As shown in Fig. 1c, the state preparation protocol consists of three steps: reset to $|00\rangle$, initialization in a logical state and optional 'check' measurements to verify the state preparation, which can boost the preparation fidelity by flagging failures for post-selection. Although there are many options for the state preparation protocol, in this work, we have utilized two different methods, with both expected to have similar performance (Supplementary Section V provides additional information). For SPAM experiments described in this section, we use an optimal control pulse[51] to initialize a cavity in $|1\rangle$ and a single transmon measurement after the optimal control pulse to check that the transmon is in $|g\rangle$, as intended. For subsequent experiments in this work, we adopt a state preparation protocol that not only includes a transmon state check but also repeated cavity state check measurements. Importantly, for our SPAM protocols, any errors in the state preparation not caught by the check measurements can still be detected later in the logical measurement as an erasure, which results in an increase in the erasure rate, but without necessarily impacting the fidelity of the logical outcome.

In our experiment, the logical measurement is simultaneously implemented by measuring both cavities to determine whether the dual-rail cavity qubit state is $|01\rangle, 10\rangle$ or a leakage state. For each cavity, we first perform a photon-number selective π pulse to map the state of the cavity onto the transmon, flipping the transmon to $|e\rangle$ only if the cavity is in $|1\rangle$. This is followed by a standard dispersive readout of the transmon, with a total duration of 4.8 μs for this sequence. There are many options for implementing the logical measurement and our chosen mapping operation is optimized for the detection of the dominant leakage state—$|00\rangle$ (Supplementary Section IV provides more details). In addition to leakage, any single ancilla error during the dual-rail logical measurement, including those arising from decoherence, control pulses or transmon readout, results not in a logical misassignment but rather in an erasure assignment. Importantly, as these photon-number resolving measurements are non-demolition on the cavity photon number[50,52], cavity measurements may be repeated to form multiple rounds of measurements to further suppress assignment errors. In this case, after each round of cavity measurements, we reset both transmons to $|g\rangle$ by applying a conditional π pulse if either transmon was found in $|e\rangle$ and append a subsequent transmon check to confirm the correct reset of the transmon. Finally, before the first logical measurement, we perform transmon readouts to verify that both are in the ground state, also assigning failures as an erasure.

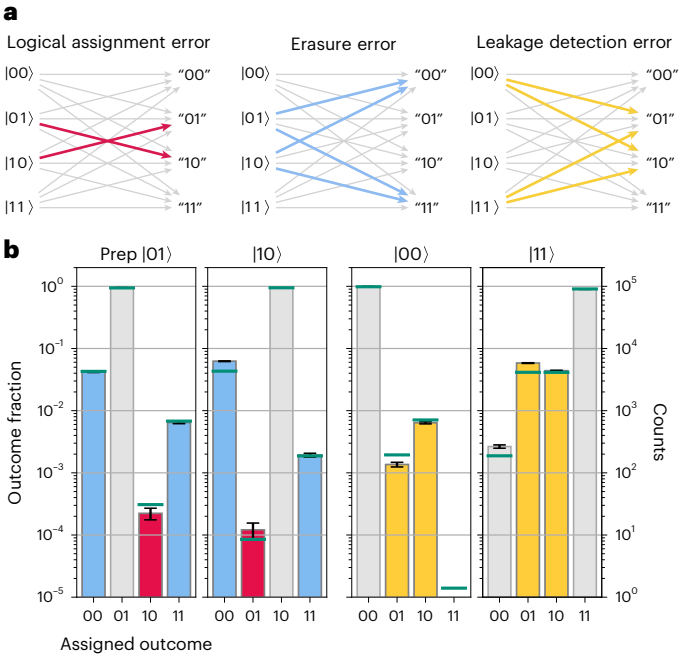

Fig. 2 | SPAM of a dual-rail qubit. a, Set of possible measurement outcomes can be summarized in the assignment channel diagram, colour coded to highlight several different figures of merit. Logical assignment errors (pink) correspond to the misassignment of basis states $|01\rangle$ for $|10\rangle$ as '10' and '10', respectively. Erasure errors (blue) indicate that an erasure outcome ('00' or '11') was measured despite preparation in one of the logical states ($|01\rangle$ or $|10\rangle$). Finally, leakage detection errors (yellow) are misassignments of a known leaked state, assigning '01' or '10' to the leakage state $|00\rangle$ or $|11\rangle$, respectively. **b**, State assignment data using one round of measurement. In our SPAM experiment, we prepare each of the four dual-rail states and perform a logical measurement. The results for each dual-rail state are shown in each panel; each bar corresponds to a different assigned physical state. The model results are shown as green lines for each outcome. For each state, we repeat the experiment for a total of 100,000 times. The height of each bar and the centre of the black line correspond to the mean of the data and the error bars represent the standard error, showing ±1σ.

Because the logical measurement protocol consists of one or more rounds of cavity measurements, each of which extracts one or more bits of information, a variety of decoding strategies can be used to assign a logical outcome: 0_L, 1_L or erasure (the 'Decoding measurement outcomes' section provides more details). Each round of cavity measurements results in raw outcomes of the transmon readouts from which we assign one of the four possible physical outcomes: {'00', '01', '10', '11'} (see Fig. 1c). In the case of a single-round logical measurement, we can directly assign the logical state: '01'→0_L, '10'→1_L and {'00', '11'}→erasure. In the case of multiple rounds, we select a decoding strategy (the 'Decoding measurement outcomes' section provides more details) to assign the most likely cavity state; in the event that a cavity state cannot be assigned, for example, if the measurement outcomes disagree, we declare an ambiguous outcome 'A', which is subsequently labelled as a logical erasure. Finally, we discard the assigned erasures and compute the logical outcome 1_L (0_L), defined as $P_{1_L(0_L)} = N_{1_L(0_L)}/(N_{0_L} + N_{1_L})$, where N is the number of shots of the assigned logical state. Given our

https://doi.org/10.1038/s41567-024-02539-4

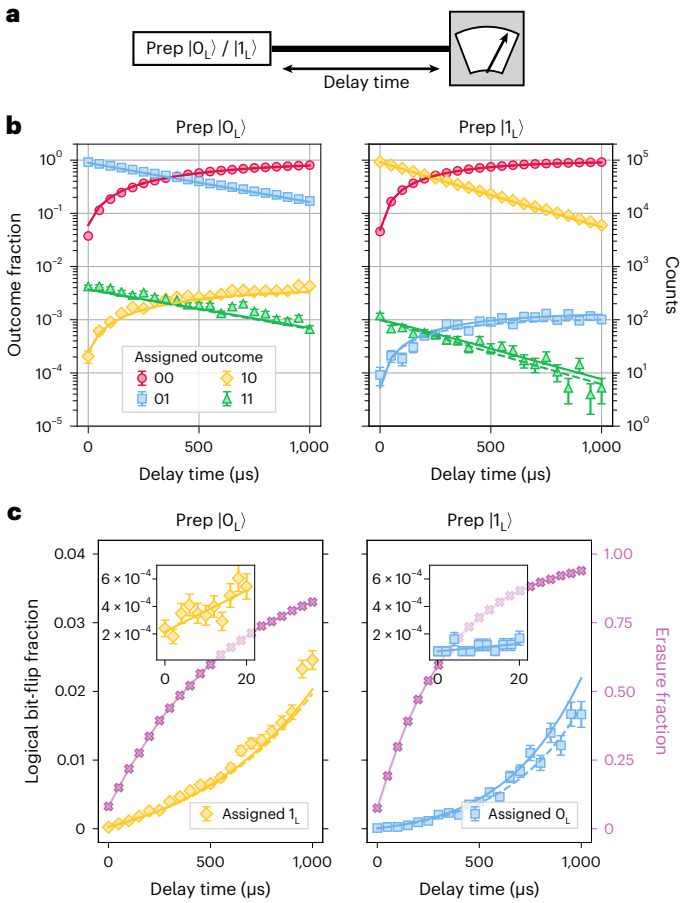

Fig. 3 | Dual-rail bit-flip error measurement. a, Measurement of the bit-flip error rate starts with logical dual-rail state preparation in either $|0_L\rangle = |01\rangle$ or $|1_L\rangle = |10\rangle$, followed by a variable delay time, and concludes with a dual-rail logical measurement. **b**, Assigned physical state outcomes measured as a function of delay for the dual-rail cavity qubit prepared in $|0_L\rangle$ (left) and $|1_L\rangle$ (right). The occurrence of each measured outcome is shown as a fraction (left axis) and as total counts (right axis). For each state preparation, we repeat the experiment for a total of 100,000 times. The solid line corresponds to a simulation performed with measured parameters, whereas the dashed line is a simulation performed without any intrinsic bit-flip errors by setting the cavity-heating rates to zero. The close overlap of the solid and dashed simulation lines indicate that the cavity heating is not the dominant error mechanism, whereas the close overlap of both simulation curves with the data gives us confidence in our understanding of the overall underlying error mechanisms. **c**, From the data in **b**, we compute the logical outcomes and plot the bit-flip error fraction when initializing in $|0_L\rangle$ (left) and $|1_L\rangle$ (right). The solid and dashed lines are generated using the same simulations as in **b**, showing the results with nominal and with no intrinsic bit-flip errors, respectively. The small difference between the two simulations provide evidence that intrinsic bit-flip errors are yet a small contribution to the apparent bit-flip error. The inset shows the results for an additional experiment performed with delays up to 20 μs. We perform a linear fit (solid line) and extract an apparent bit-flip error probability of $(1.5 \pm 0.4) \times 10^{-5}$ and $(3.0 \pm 1.0) \times 10^{-6}$ in a microsecond for $|0_L\rangle$ (left) and $|1_L\rangle$ (right), respectively. The error bars for all the data represent the standard error, showing $\pm 1\sigma$.

mapping choice, each cavity measurement informs us whether or not the cavity is in $|1\rangle$. Higher leakage states in an individual cavity, such as $|2\rangle$, whereas less likely, are nonetheless assigned to outcome '0'. As such, dual-rail cavity qubit leakage states, such as $|02\rangle$ or $|20\rangle$, will be assigned to '00' and labelled as an erasure.

We characterize our logical SPAM by quantifying logical misassignment errors and demonstrating the unique erasure detection capability of our logical measurement. We perform our SPAM experiment by preparing logical states $|0_L\rangle = |01\rangle$ and $|1_L\rangle = |10\rangle$ and then performing a logical measurement. From this experiment, we extract two figures of merit. First, the logical misassignment error is defined as the fraction of counts assigned to '10' ('01') when preparing $|01\rangle$ ($|10\rangle$); this is represented by the assignment channel shown with the pink arrows in Fig. 2a. From our data (Fig. 2b, pink bars), we determine the logical misassignment error to be $(1.8 \pm 0.3) \times 10^{-4}$, averaged over both state preparations. Second, we can quantify the erasure fraction as the relative number of counts labelled '00' or '11' (channel shown in blue arrows in Fig. 2a), which we measure to be $(6.03 \pm 0.05) \times 10^{-2}$ (Fig. 2b, blue bars). In addition to preparation errors, which are a logical leakage error, assigned erasures can also arise from any single error during the dual-rail measurement, including leakage in a cavity, transmon decoherence or readout errors. False erasure assignments, for which the dual-rail cavity qubit is still in the code space, are false positives and set a lower bound on the erasure fraction.

By intentionally preparing leakage states $|00\rangle$ and $|11\rangle$, we directly test the erasure detection capability of our logical measurement. This assignment channel is shown in Fig. 2a (yellow arrows) and the experimental results are shown in Fig. 2b (right). The critical figure of merit is what we call the leakage detection error, which is the fraction of false negatives, that is, when we fail to detect a leakage event. Because undetected leakage errors are amongst the most damaging errors in a stabilizer code, it is important to keep the fraction of leaked qubits small[53–56]. In our system, photon loss from the code space to $|00\rangle$ is by far the dominant leakage channel, and we measure a leakage detection error of $(7.7 \pm 0.3) \times 10^{-3}$. As such, we can convert more than 99% of leakage errors into erasures. The leakage detection error when preparing $|11\rangle$ is higher (at the 10^{-2} level), but leakage to this state is much rarer, at least 1,000 times less likely, requiring a cavity-heating event.

We have developed a detailed model to simulate the SPAM protocol (Supplementary Section VIII), finding close agreement between these simulations (Fig. 2b, green lines) and our experimental data. Further, we have developed a simplified error model (Supplementary Section IX provides more details) to determine the physical error mechanisms that contribute to incorrectly assigned outcomes. Using this model, we infer that outcomes assigned as erasures are often transmon T_1 events during readout, contributing between 30–50% of the total error. Leakage detection errors are dominated by transmon readout classification errors, contributing between 60% and 90% of the total error.

Finally, by performing the SPAM experiment with two rounds of measurements, we observe an exceedingly low logical misassignment error of $(4 \pm 2) \times 10^{-5}$ and leakage detection error of $(1.2 \pm 0.1) \times 10^{-3}$ (Extended Data Fig. 2). We attribute this almost five times improvement to the decoding strategy where we require agreement between both rounds of measurements (the 'SPAM experiment using two rounds of measurements' section provides more details). Such a strategy suppresses the effect of ancilla errors on logical misassignment and leakage detection error, instead assigning these outcomes as additional erasures. We do observe this trade-off and report a higher erasure fraction, measured in our system to be $(17 \pm 0.1) \times 10^{-2}$. Nevertheless, this experiment highlights the flexibility of our measurement protocol, with options for multiple rounds of measurements and strategies for reduced SPAM error or for reduced erasures.

Measuring bit-flip errors

Having demonstrated a high-fidelity logical measurement, we now use this tool to probe idling errors in our dual-rail qubit. First, we study the dual-rail bit-flip error rate, defined here as the rate of transition from one logical state to the other: $|01\rangle \rightarrow |10\rangle$, and vice versa. We expect these transitions to be exceedingly rare, caused by a double error via photon loss in one cavity and photon gain in the other cavity, thereby inducing a bit flip in the logical state. In our system, Alice and Bob cavities have relaxation times of $T_1 = 1/\kappa = 592$ and 350 μs and thermal populations of $n_{th} = 3.5 \times 10^{-4}$ and 1.7×10^{-4}, respectively (Supplementary Section

https://doi.org/10.1038/s41567-024-02539-4

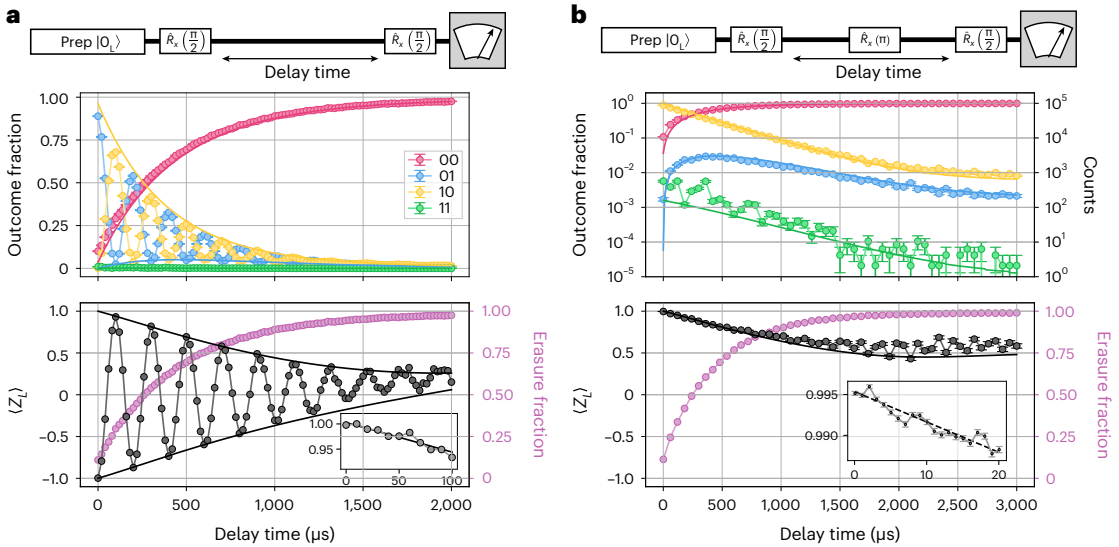

Fig. 4 | Dual-rail phase error measurement. a,**b**, Dual-rail qubit Ramsey (**a**) and echo (**b**) experiment, with the top panel showing the dual-rail circuit used to measure the dephasing error rates. The middle panel shows the assigned physical outcomes, and the bottom panel shows the logical outcome $\langle \hat{Z}_L \rangle$ (black) and erasure fraction (purple). The simulation results are shown in the solid lines. The inset shows the results from an additional experiment performed with shorter delays and the black line is a linear fit to the data. We extract the phase-flip error probabilities of (0.023 ± 0.003)% and (0.019 ± 0.001)% in a microsecond for the Ramsey and echo experiments, respectively. For both these experiments, we repeat the experiment for a total of 100,000 times. The error bars represent the standard error (±1σ).

I provides more details). In this experiment (Fig. 3a), the qubit is prepared in either of the logical states, namely, $|0_L\rangle \equiv |01\rangle$ (photon in Alice) or $|1_L\rangle \equiv |10\rangle$ (photon in Bob), and a logical measurement is performed after a variable delay.

We first consider the assigned physical outcomes (Fig. 3b). At zero delay, the assigned outcomes are consistent with the $|01\rangle$ and $|10\rangle$ SPAM results, and we find the probability of assigning the bit-flip outcome to be ~10^{-4}. As the delay increases, we observe the expected exponential increase in the $|00\rangle$ population (Fig. 3b, red markers) due to decay errors out of the code space. At longer delay times, the assigned outcomes tend towards the measurement outcomes when preparing $|00\rangle$, as shown in our SPAM experiment. Our apparent bit-flip rate will have contributions from the intrinsic bit-flip error rate, defined as the logical transition rate in the absence of logical assignment errors, as well as from leakage detection errors. We compare our data with two simulations, one with the measured hardware parameters and the other with no intrinsic bit-flip errors by setting the cavity thermal populations $n_{th} = 0$ (Fig. 3b, solid and dashed lines, respectively). We find that both simulations agree well with the data, suggesting that the bit-flip outcome counts are not dominated by actual state transitions in the cavities but rather by measurement errors.

From the assigned physical outcomes, we plot the logical bit-flip outcomes (Fig. 3c). We also plot the erasure fraction, and find that it is consistent with the individual cavity decay rates. We define the dual-rail erasure probability in a microsecond to be given by the average of the cavity decay rates, $\bar{\kappa} = (\kappa_A + \kappa_B)/2 = 1/(440\ \mu s)$. Given the high-fidelity logical measurement, we also perform these experiments at short times (20 μs) to directly observe idling errors on the few-microsecond timescale relevant for a logical entangling gate[46]. We perform a linear fit to the short-time data, and show that the probability of apparent logical errors is (0.0015 ± 0.0004)% and (0.0003 ± 0.0001)% in 1 μs when preparing $|0_L\rangle$ and $|1_L\rangle$, respectively. These correspond to effective bit-flip rates of 1/(66 ± 16 ms) and 1/(364 ± 189 ms). Finally, we quantify the ratio between erasure errors and bit-flip error rate to conservatively be higher than $(440\ \mu s)^{-1}/(66\ ms)^{-1} = 150$.

Our model suggests that this rate is an upper bound on the intrinsic dual-rail bit-flip rate, as the intrinsic bit-flip contributes only ~0.5% of the apparent bit flip even at 20 μs (Supplementary Section X provides more details). Given the good agreement with the simulation, we infer that the intrinsic bit-flip rate should be non-exponential[37] and extremely slow, with a probability of ~$n_{th}(\kappa t)^2$ at short times, which would be only a few parts per billion in a microsecond (Supplementary Section IX.B).

Measuring dephasing rates

We perform Ramsey and echo experiments to make the first estimate of phase errors of the dual-rail cavity qubit. This measurement is particularly important as the efficacy of dual-rail encoding relies on preserving the low dephasing errors of the individual cavities when adding additional nonlinear elements. After state preparation in a logical dual-rail state ($|0_L\rangle \equiv |01\rangle$ (photon in Alice)), the Ramsey sequence is performed by applying a logical π/2 pulse, implemented via a parametric beamsplitter interaction[44,45], and, after a variable delay, applying a second logical π/2 pulse, before measuring the qubit. In the case of the echo measurement, an additional logical π pulse is inserted midway during the delay. For the Ramsey experiment, the beamsplitter is intentionally detuned by a small (5 kHz) amount, giving rise to the periodic behaviour of the superposition of states.

We present the results of the Ramsey and echo dephasing experiments (Fig. 4). In both the experiments, we observe a decrease in the expectation value of $\hat{Z}_L = |1_L\rangle\langle 1_L| - |0_L\rangle\langle 0_L|$, which is consistent with the dephasing of the logical state. However, one difference that we observe in our data is an offset in $\langle \hat{Z}_L \rangle$ at long times, where it is expected to decay to zero. This can be explained by leakage detection errors that bias the logical measurement at long times, due to the increased probability of being in the $|00\rangle$ state. As the delay time increases, the probability that the system suffers a decay error to $|00\rangle$ also increases. With this increased probability of being in $|00\rangle$, there is an increased contribution of the measurement outcome from leakage detection error (see the 'Characterizing dual-rail SPAM' section) where state $|00\rangle$ is misassigned as a '01' or '10' outcome with unequal probabilities. Our modelling suggests that this is the dominant effect at long times ($t \gg T_1$) and causes the apparent bias in the data. We provide further discussion of this effect in Supplementary Section VII. To limit the impact of this

measurement error, we perform coherence experiments at shorter delay times, which again allows us to extract the error rates on the few-microsecond timescale relevant for dual-rail entangling gate. For these short-time Ramsey experiments, we implement an extended version of this experiment where, in addition to varying the Ramsey delay, we sweep the phase of the second π/2 pulse (the 'Short-time Ramsey experiment' section provides more details). From these experiments, we extract the dephasing rates from the linear slope of $\Gamma_\phi^{\mathrm{R}} = 1/(2.2 \pm 0.2\,\mathrm{ms})$and $\Gamma_\phi^{\mathrm{E}} = 1/(2.7 \pm 0.2\,\mathrm{ms})$, respectively, for Ramsey and echo. From these quantities, we infer the phase-flip error probabilities as $p_\phi = \Gamma_\phi t/2$ for time t, for Ramsey and echo of $p_\phi^{\mathrm{R}} = (0.023 \pm 0.003)\%$ and $p_\phi^{\mathrm{E}} = (0.019 \pm 0.001)\%$ in a microsecond, respectively (Supplementary Section VI provides more details). Using these measured dual-rail dephasing rates in our simulations of the Ramsey and echo experiments, we indeed find good agreement with the long-time dephasing behaviour. The reported dual-rail dephasing rates are probably still dominated by extrinsic sources, introduced by finite heating rates and state transitions of the dispersively coupled nonlinear elements, which are two measurement transmons and three Josephson coupling elements in our system (Fig. 1b). This initial bound on the phase-flip rate measured here is encouraging, and the extracted error rates for the Ramsey and echo experiment are five and six times slower than the erasure rate, respectively. Further improvements are achievable, for example, by decreasing the heating rates in these elements and detecting their residual state transitions as erasures.

Conclusion

We have developed a logical measurement with built-in erasure detection resulting in logical misassignment on the order of 10^{-4} and with efficiency for detecting leakage to $|00\rangle$ in excess of 99%. Our measurements show that the logical bit-flip rate is at least two orders of magnitude smaller than the erasure rate, and that the logical phase-flip rate is a factor of six smaller, providing initial confirmation that dual-rail cavity qubits can have a favourable hierarchy of errors in the idling state. Further improvements in the measurement and characterization of dual-rail qubits should also be possible. First, although we have already demonstrated low error rates, a more detailed analysis of the physical phenomena and the ultimate limits on dephasing in the dual-rail qubit are key questions and a topic of ongoing investigations. Second, this logical measurement can be used as a syndrome measurement for a stabilizer code and in such an application, it will be important to minimize the erasure fraction. Our analysis (Supplementary Section IX) indicates that a substantial fraction of erasure assignments are false positives and can be improved by further hardware optimizations. Finally, asymmetric errors in erasure detection can introduce a bias in the measured outcomes, particularly for longer circuits where the erasure fraction is high, and therefore, ways to estimate and mitigate these effects should be pursued.

We have demonstrated high-fidelity SPAM in the logical Z basis of an encoded dual-rail cavity qubit—a fundamental building block required to operate these qubits for any purpose. Furthermore, this will serve as a foundational tool for the characterization of subsequent dual-rail operations such as entangling gates and mid-circuit erasure detection. This low SPAM error allows a direct characterization of logical operations without having to resort to techniques to mitigate physical measurement errors, such as randomized benchmarking, which have been necessary given high SPAM errors relative to gate errors. Combining the already demonstrated dual-rail operations—single-qubit gates[44,45] and SPAM—with mid-circuit erasure detection and proposed two-qubit entangling gates[46] would complete a full toolbox of error-detected quantum operations for the dual-rail cavity architecture.

Moving beyond error detection to full error correction with erasure qubits requires using dual-rail qubits as physical qubits in a stabilizer code. Leakage detection in a single dual-rail qubit is an important first step on the path to correct erasures, which will require a next-level code made by concatenating many dual-rail qubits. Further exploration and confirmation of the expected error hierarchy—during not only idling but operations—could, therefore, enable a new and faster path to fault-tolerant computing. Finally, the ability to convert errors into measurable erasures also creates near-term opportunities for error mitigation and improved fidelity in short-depth circuits.

Note: During completion of this manuscript, we became aware of related work on the dual-rail encoding using tunable transmon qubits[47].

Online content

Any methods, additional references, Nature Portfolio reporting summaries, source data, extended data, supplementary information, acknowledgements, peer review information; details of author contributions and competing interests; and statements of data and code availability are available at https://doi.org/10.1038/s41567-024-02539-4.

References

1. Mirrahimi, M. et al. Dynamically protected cat-qubits: a new paradigm for universal quantum computation. *New J. Phys.* **16**, 045014 (2014).
2. Michael, M. H. et al. New class of quantum error-correcting codes for a bosonic mode. *Phys. Rev. X* **6**, 031006 (2016).
3. Joshi, A., Noh, K. & Gao, Y. Y. Quantum information processing with bosonic qubits in circuit QED. *Quantum Sci. Technol.* **6**, 033001 (2021).
4. Cai, W., Ma, Y., Wang, W., Zou, C.-L. & Sun, L. Bosonic quantum error correction codes in superconducting quantum circuits. *Fundam. Res.* **1**, 50–67 (2021).
5. Ma, W.-L. et al. Quantum control of bosonic modes with superconducting circuits. *Sci. Bull.* **66**, 1789–1805 (2021).
6. Ofek, N. et al. Extending the lifetime of a quantum bit with error correction in superconducting circuits. *Nature* **536**, 441–445 (2016).
7. Sivak, V. V. et al. Real-time quantum error correction beyond break-even. *Nature* **616**, 50–55 (2023).
8. Ni, Z. et al. Beating the break-even point with a discrete-variable-encoded logical qubit. *Nature* **616**, 56–60 (2023).
9. Hu, L. et al. Quantum error correction and universal gate set operation on a binomial bosonic logical qubit. *Nat. Phys.* **15**, 503–508 (2019).
10. Aliferis, P. & Preskill, J. Fault-tolerant quantum computation against biased noise. *Phys. Rev. A* **78**, 052331 (2008).
11. Tuckett, D. K. et al. Tailoring surface codes for highly biased noise. *Phys. Rev. X* **9**, 041031 (2019).
12. Guillaud, J. & Mirrahimi, M. Repetition cat qubits for fault-tolerant quantum computation. *Phys. Rev. X* **9**, 041053 (2019).
13. Darmawan, A. S., Brown, B. J., Grimsmo, A. L., Tuckett, D. K. & Puri, S. Practical quantum error correction with the XZZX code and Kerr-cat qubits. *PRX Quantum* **2**, 030345 (2021).
14. Claes, J., Bourassa, J. E. & Puri, S. Tailored cluster states with high threshold under biased noise. *npj Quantum Inf.* **9**, 9 (2023).
15. Aliferis, P. et al. Fault-tolerant computing with biased-noise superconducting qubits: a case study. *New J. Phys.* **11**, 013061 (2009).
16. Grimm, A. et al. Stabilization and operation of a Kerr-cat qubit. *Nature* **584**, 205–209 (2020).
17. Puri, S. et al. Bias-preserving gates with stabilized cat qubits. *Sci. Adv.* **6**, eaay5901 (2020).
18. Lescanne, R. et al. Exponential suppression of bit-flips in a qubit encoded in an oscillator. *Nat. Phys* **16**, 509–513 (2020).
19. Berdou, C. et al. One hundred second bit-flip time in a two-photon dissipative oscillator. *PRX Quantum* **4**, 020350 (2023).
20. Chao, R. & Reichardt, B. W. Flag fault-tolerant error correction for any stabilizer code. *PRX Quantum* **1**, 010302 (2020).

21. Chamberland, C., Zhu, G., Yoder, T. J., Hertzberg, J. B. & Cross, A. W. Topological and subsystem codes on low-degree graphs with flag qubits. *Phys. Rev. X* **10**, 011022 (2020).
22. Ryan-Anderson, C. et al. Realization of real-time fault-tolerant quantum error correction. *Phys. Rev. X* **11**, 041058 (2021).
23. Ryan-Anderson, C. et al. Implementing fault-tolerant entangling gates on the five-qubit code and the color code. Preprint at https://arxiv.org/abs/2208.01863 (2022).
24. Chen, E. H. et al. Calibrated decoders for experimental quantum error correction. *Phys. Rev. Lett.* **128**, 110504 (2022).
25. Wu, Y., Kolkowitz, S., Puri, S. & Thompson, J. D. Erasure conversion for fault-tolerant quantum computing in alkaline earth Rydberg atom arrays. *Nat. Commun.* **13**, 4657 (2022).
26. Kubica, A. et al. Erasure qubits: overcoming the T_1 limit in superconducting circuits. *Phys. Rev. X* **13**, 041022 (2023).
27. Kang, M., Campbell, W. C. & Brown, K. R. Quantum error correction with metastable states of trapped ions using erasure conversion. *PRX Quantum* **4**, 020358 (2023).
28. Ma, S. et al. High-fidelity gates and mid-circuit erasure conversion in an atomic qubit. *Nature* **622**, 279–284 (2023).
29. Scholl, P. et al. Erasure conversion in a high-fidelity Rydberg quantum simulator. *Nature* **622**, 273–278 (2023).
30. Grassl, M., Beth, T. & Pellizzari, T. Codes for the quantum erasure channel. *Phys. Rev. A* **56**, 33 (1997).
31. Stace, T. M., Barrett, S. D. & Doherty, A. C. Thresholds for topological codes in the presence of loss. *Phys. Rev. Lett.* **102**, 200501 (2009).
32. Barrett, S. D. & Stace, T. M. Fault tolerant quantum computation with very high threshold for loss errors. *Phys. Rev. Lett.* **105**, 200502 (2010).
33. Chuang, I. L. & Yamamoto, Y. Simple quantum computer. *Phys. Rev. A* **52**, 3489 (1995).
34. Knill, E., Laflamme, R. & Milburn, G. J. A scheme for efficient quantum computation with linear optics. *Nature* **409**, 46–52 (2001).
35. Kok, P. et al. Linear optical quantum computing with photonic qubits. *Rev. Mod. Phys.* **79**, 135 (2007).
36. Bartolucci, S. et al. Fusion-based quantum computation. *Nat. Commun.* **14**, 912 (2023).
37. Teoh, J. D. et al. Dual-rail encoding with superconducting cavities. *Proc. Natl Acad. Sci. USA* **120**, e2221736120 (2023).
38. Zakka-Bajjani, E. et al. Quantum superposition of a single microwave photon in two different 'colour' states. *Nat. Phys.* **7**, 599–603 (2011).
39. Shim, Y.-P. & Tahan, C. Semiconductor-inspired design principles for superconducting quantum computing. *Nat. Commun.* **7**, 11059 (2016).
40. Campbell, D. L. et al. Universal nonadiabatic control of small-gap superconducting qubits. *Phys. Rev. X* **10**, 041051 (2020).
41. Rosenblum, S. et al. Fault-tolerant detection of a quantum error. *Science* **361**, 266–270 (2018).
42. Reinhold, P. et al. Error-corrected gates on an encoded qubit. *Nat. Phys.* **16**, 822–826 (2020).
43. Ma, Y. et al. Error-transparent operations on a logical qubit protected by quantum error correction. *Nat. Phys.* **16**, 827–831 (2020).
44. Chapman, B. J. et al. High-on-off-ratio beam-splitter interaction for gates on bosonically encoded qubits. *PRX Quantum* **4**, 020355 (2023).
45. Lu, Y.et al. High-fidelity parametric beamsplitting with a parity-protected converter. *Nat. Commun.* **14**, 5767 (2023).
46. Tsunoda, T. et al. Error-detectable bosonic entangling gates with a noisy ancilla. *PRX Quantum* **4**, 020354 (2023).
47. Levine, H. et al. Demonstrating a Long-Coherence Dual-Rail Erasure Qubit Using Tunable Transmons. *Phys. Rev. X* **14**, 011051 (2024).
48. Koottandavida, A. et al. Erasure detection of a dual-rail qubit encoded in a double-post superconducting cavity. *Phys. Rev. Lett.* **132**, 180601 (2024).
49. Gambetta, J., Braff, W. A., Wallraff, A., Girvin, S. M. & Schoelkopf, R. J. Protocols for optimal readout of qubits using a continuous quantum nondemolition measurement. *Phys. Rev. A* **76**, 012325 (2007).
50. Elder, S. S. et al. High-fidelity measurement of qubits encoded in multilevel superconducting circuits. *Phys. Rev. X* **10**, 011001 (2020).
51. Heeres, R. W. et al. Implementing a universal gate set on a logical qubit encoded in an oscillator. *Nat. Commun.* **8**, 94 (2017).
52. Curtis, J. C. et al. Single-shot number-resolved detection of microwave photons with error mitigation. *Phys. Rev. A* **103**, 023705 (2021).
53. Fowler, A. G. Coping with qubit leakage in topological codes. *Phys. Rev. A* **88**, 042308 (2013).
54. Ghosh, J., Fowler, A. G., Martinis, J. M. & Geller, M. R. Understanding the effects of leakage in superconducting quantum-error-detection circuits. *Phys. Rev. A* **88**, 062329 (2013).
55. Bultink, C. C. et al. Protecting quantum entanglement from leakage and qubit errors via repetitive parity measurements. *Sci. Adv.* **6**, eaay3050 (2020).
56. McEwen, M. et al. Removing leakage-induced correlated errors in superconducting quantum error correction. *Nat. Commun.* **12**, 1761 (2021).

[1]Quantum Circuits, Inc., New Haven, CT, USA. [2]Departments of Applied Physics and Physics, Yale University, New Haven, CT, USA. [3]Yale Quantum Institute, Yale University, New Haven, CT, USA. [4]National Institute of Standards and Technology, Boulder, CO, USA. ✉e-mail: chou@quantumcircuits.com; robert.schoelkopf@yale.edu

Methods

Decoding measurement outcomes

In this section, we discuss our methodology for decoding measurement outcomes for our dual-rail experiments. The assignment of physical and logical outcomes for a dual-rail experiment is more involved than that of a transmon given that each dual-rail sequence can involve multiple measurements of both cavities and transmons. Our state preparation and logical measurement protocols consist of a number of 'check' measurements as well as the logical measurement (Supplementary Section V). In the state preparation protocol, state initialization is followed by a transmon check and an optional sequence of cavity check measurements. For the logical dual-rail measurement, we first perform a transmon check and then perform the logical cavity measurement. In the case of multiple rounds, we will reset the transmons after each round of logical cavity measurement and perform an additional transmon measurement to check that the transmons are in the ground state. Extended Data Fig. 1a shows the sequence of measurements.

We group the checks and logical measurements into three categories, determined by the ways in which we use the outcomes to classify each of the runs of the experiment: failed state preparation check (FPC), failed measurement check (FMC) and failed state assignment (FA). Although FPC shots are removed from the total number of counts, FMC and FA shots contribute to the erasure counts (Extended Data Fig. 1b). In this section, we describe each of these three categories and the way in which we analyse the counts assigned from each category.

1. FPC: after initializing the dual-rail state, we perform measurements of the ancilla transmons order to confirm that they are both in $|g\rangle$. Optionally, we can also perform a subsequent sequence of cavity measurements to confirm the correct preparation of the cavity state. If in any run of the experiment, the transmon checks indicate that either of the transmons were in $|e\rangle$ or if (in the case where cavity checks were performed) any of the cavity measurements indicate that either of the cavities were not in the intended state, then the shot is labelled as 'FPC' and removed from the total number of counts.
   In other words, if N_{All} is the number of shots that were performed, the total number of counts that we consider (N_{T}) is as follows.
$$N_{\mathrm{T}} = N_{\mathrm{All}} - N_{\mathrm{FPC}}$$
2. FMC: before performing the logical end-of-the-line measurement, we perform measurements of the ancilla transmons to confirm that they are both in $|g\rangle$ before the logical measurement. In the case where we perform multiple rounds of logical measurements, we also perform a transmon check before each additional logical measurement to confirm that the transmon reset after the previous measurement was successful, and that both transmons are indeed in $|g\rangle$ before the next logical measurement. If any of these checks indicate that either of the transmons were in $|e\rangle$, and if the shot was not already labelled as FPC, then the shot is labelled as FMC, giving us counts of N_{FMC} and will contribute to the erasure fraction.
3. FA: FA can get assigned from the logical measurements when multiple rounds of measurements are performed. Following the state assignment method (main text), using the results of the logical measurements, we can assign one of the four outcomes, namely, {'00', '01', '10', '11'}, giving us the counts for N_{00}, N_{01}, N_{10} and N_{11}, respectively. However, if two measurements do not agree in the case where we perform two rounds of measurements or if there is no strict majority in the case where we perform more than two measurements, the outcome is ambiguous and labelled as FA, giving us the N_{FA} counts.

Having defined all types of count that we can assign from the ensemble of shots of an experiment, we can explicitly define each of the SPAM metrics described in the main text.

The logical misassignment error when preparing $|01\rangle$ ($|10\rangle$) is defined as
$$\frac{N_{10(01)}}{N_{10}+N_{01}}.$$
The erasure fraction is defined as
$$\frac{N_{\mathrm{FMC}}+N_{00}+N_{11}+N_{\mathrm{FA}}}{N_{\mathrm{T}}},$$
where $N_{\mathrm{FA}}=0$ in the case where only one logical measurement is performed. Finally, the leakage detection error to the logical state $|0_{\mathrm{L}}\rangle$ ($|1_{\mathrm{L}}\rangle$), measured by intentionally preparing $|00\rangle$ and $|11\rangle$, is defined as
$$\frac{N_{01(10)}}{N_{\mathrm{T}}}.$$

SPAM experiment using two rounds of measurements

We discuss the results for the SPAM experiment with two rounds of measurements, that is, $N_{\mathrm{rounds}}=2$. Our strategy for decoding the measurement results is to require that both raw measurement outcomes agree to assign a physical state outcome {'00', '01', '10', '11'}; if the raw measurement outcomes disagree, for example, we observe the two-round sequence ('GE', 'GG'), then we assign an ambiguous outcome 'A' and subsequently assign as a logical erasure. With this measurement protocol, we measure a logical misassignment error of $(4\pm2)\times10^{-5}$, leakage detection error of $(1.2\pm0.1)\times10^{-3}$ and erasure fraction of $(17.0\pm0.1)\times10^{-2}$. With multiple rounds of measurements, the contributions to the total erasure fraction comes from both assigned erasure states '00' and '11', and from the ambiguous assignments 'A'.

As described in the main text, SPAM errors can arise either from state preparation errors, cavity transitions or from physical ancilla errors during the two rounds of measurements. From our error analysis, we find that cavity transitions are not the dominant source of SPAM errors, which are instead dominated by physical ancilla errors and state preparation errors (Supplementary Section IX). Physical ancilla errors such as errors during the cavity-state mapping or during the dispersive readout will result in an incorrect assignment of the underlying cavity state. By performing two rounds of measurements, the impact of these physical errors on the state assignment is suppressed, as the probability of such an error occurring on both consecutive measurements and corrupting the assignment is p^2 rather than p, where p is the probability of a transmon ancilla error.

With this in mind, we can understand the ways in which the two rounds of measurements affect each of the three figures of merit that we extract from the SPAM experiment. First, we expect the logical assignment error to decrease. A logical misassignment is a second-order logical error resulting from an error in both cavities. Suppressing each of the cavity misassignment probabilities to p^2 means that the logical misassignment due to ancilla errors becomes a highly unlikely fourth-order event that can result only from the consecutive misassignment of both cavities. On the other hand, errors due to state preparation or cavity transitions between the state preparation and logical measurement will not be suppressed by multiple measurements as the logical measurement is quantum non-demolition and, as such, any number of measurements should result in outcomes that agree and as such cannot be 'caught'. For instance, from our error model (Supplementary Section IX), we find that the dominant error channel contributing to logical assignment errors with two rounds of measurements is the case where one of the dual-rail's cavities are misassigned with both post-cavity-state mapping readout and post-reset transmon check, and suffer a state preparation error on the other cavity.

Second, we expect the leakage detection error to decrease slightly. On one hand, the probability of actual leakage during the two

measurements increases by a factor of 2, that is, the probability of a cavity-state transition increases from ~t_{RM}/T_1 to ~$2t_{RM}/T_1$, where t_{RM} is the duration of each round of measurement. However, as a subset of the leakage detection errors are the result of misassignment due to ancilla errors, these errors will be suppressed by a power of 2 by the second measurement, offsetting the increase in actual leakage errors.

Finally, we expect the erasure fraction to increase due to two primary contributions compared with the erasure fraction from one round of measurement. First, with our decoding strategy, any two-round outcomes that disagree with one another are decoded as 'A' and contribute to the erasure fraction. In such cases, if the outcome of the first round of measurement is '00' or '11', it would have contributed to the erasure fraction even in the case of one round of measurement and thus is not an additional contribution. However, cases where the result of the first round is assigned to be in the code space but the outcome of the second round is assigned as a leakage state or the opposite logical state will get decoded as residual 'A' counts compared with one round of measurement. For our system, we both estimate and measure this contribution to be ~4%. Second, as described in Supplementary Section V, after each round of measurement, the ancilla transmon is reset to $|g\rangle$ if it is measured to be in $|e\rangle$ after the cavity measurement by way of an unselective π pulse. This conditional reset is followed by a transmon check to confirm that it was correctly reset to the ground state. In cases where this check fails, the shot is treated as an erasure and is an additional contribution to the 'A' fraction, as this check is not performed in the case of a single round of measurement.

Short-time Ramsey experiment

As described in the main text, we used an extended protocol for performing a short-time Ramsey experiment to better resolve the dephasing at these shorter delays, mitigating the effects arising from small detuning errors. In this version, we vary both Ramsey delay and phase of the second π/2 pulse. For each delay, as a function of the phase of the second π/2 pulse, we extract a characteristic Ramsey oscillation in the expectation value and the coherence of the qubit is encoded in the amplitude of the oscillation. We fit and extract the contrast of the oscillation for each delay. Finally, we fit the contrast as a function of delay to extract the dephasing error rate. These results are shown in Extended Data Fig. 3.

Data availability

The datasets generated and analysed during this study are available via Zenodo at https://doi.org/10.5281/zenodo.11099521 (ref. 57).

Code availability

The code that supports the findings of this study is available from the corresponding authors upon reasonable request.

References

57. Chou, K. Datasets for 'A superconducting dual-rail cavity qubit with erasure-detected logical measurements'. *Zenodo* https://doi.org/10.5281/zenodo.11099521 (2024).

Acknowledgements

We thank the broader mechanical and control system groups at QCI, particularly C. Clothier, R. Chamberlin, M. Maxwell and C. Wehr. This research was supported by the US Army Research Office (ARO) under grant W911NF-23-1-0051, and by the US Department of Energy, Office of Science, National Quantum Information Science Research Centers, Co-design Center for Quantum Advantage (C2QA), under contract no. DE-SC0012704. The views and conclusions contained in this document are those of the authors and should not be interpreted as representing official policies, either expressed or implied, of the ARO or the US government. The US government is authorized to reproduce and distribute reprints for government purpose notwithstanding any copyright notation herein.

Author contributions

K.S.C., T.S., H.M., T.-C.C., P.L., N.M., A.N. and T.N. designed, implemented and performed the experiments. J.D.T., P.W., S.J.d.G., J.W.O.G., W.D.K., A.M., T.T. and S.H.X. contributed to the design of SPAM protocols and provided key insights into dual-rail coherence error sources. T.S., K.S.C., N.M., J.D.T., J.C.C. and T.T. contributed to the error model design and implementation. J.C.C. and T.T. provided critical insights into the design and optimization of the SPAM protocol. T.K. contributed to the single-qubit gate benchmarking. B.G., C.U.L., G.L., N.K., S.O.M. and J.O.Y. contributed to the design, fabrication and building of the experimental setup as well as initial system validation. A.A., J.C. and L.M.-K. contributed to the implementation of the software system used to perform these experiments. All work was supervised by L.F., J.A., S.P., S.M.G., S.H.M.J. and R.J.S. All authors discussed the results and contributed to the manuscript.

Competing interests

R.J.S. and L.F. are founders and shareholders of Quantum Circuits, Inc. (QCI). S.P. and S.M.G. receive consulting fees and/or are equity holders in QCI. K.S.C., T.S., H.M., T.-C.C., A.A., J.C., B.G., T.K., N.K., C.U.L., G.L., P.L., L.M.-K., N.M., S.O.M., A.N., T.N., J.O.Y., L.F., J.A., S.H.M.J. and R.J.S. have financial interest in QCI. The US patent 'Dual-rail qubits based on superconducting resonant cavities and their application for quantum error correction' has been filed (PCT/US23/84327) by R.J.S., S.M.G., S.P., J.D.T., S.J.d.G., S.H.X., B. Chapman, J.W.O.G., A.M., Y.L., W.D.K., N. Thakur, T.T. and P.W. with Yale University. The remaining authors declare no competing interests.

Additional information

Extended data is available for this paper at https://doi.org/10.1038/s41567-024-02539-4.

Supplementary information The online version contains supplementary material available at https://doi.org/10.1038/s41567-024-02539-4.

Correspondence and requests for materials should be addressed to Kevin S. Chou or Robert J. Schoelkopf.

Peer review information *Nature Physics* thanks Luyan Sun for their contribution to the peer review of this work.

https://doi.org/10.1038/s41567-024-02539-4

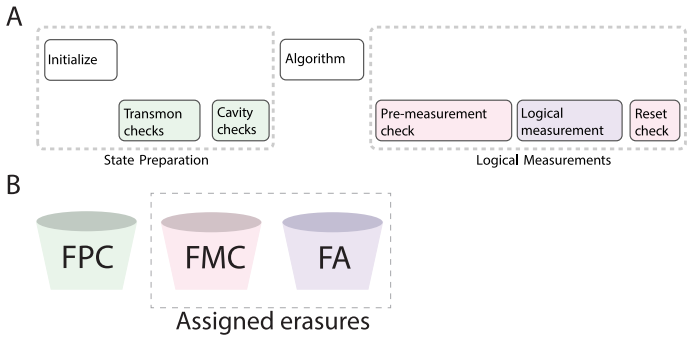

Extended Data Fig. 1 | Decoding measurement outcomes. (A) Measurement outcomes are decoded and assigned based on the results of each of the check measurements and the logical measurement is the state preparation and measurement protocols. As described in Supplementary Information Section V, there are check measurements associated with the state preparation, and check measurements associated with the logical measurement that come after a delay or an algorithm between the state preparation and measurement. The dashed lines indicate the grouping of the check measurements to state preparation or logical measurement; the colors indicate one of the three categories that are used to assign the outcomes of each of the measurements (B) The outcomes of each of the check or logical measurements can result in the shot being assigned either as FPC (failed state preparation check), FMC (failed measurement check), or FA (failed assignment). Each such k shot is placed into an abstract 'bucket', and contributes to the total counts of the outcome, N_k. N_{FPC} counts are removed from the total number of counts, while N_{FMC} and N_{FA} are two of the contributing groups of counts to the erasure fraction.

https://doi.org/10.1038/s41567-024-02539-4

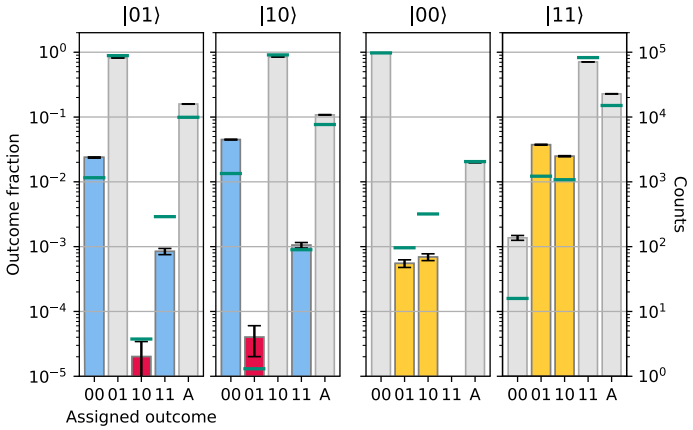

Extended Data Fig. 2 | State assignment data using 2 rounds of measurements. As in the case of the SPAM experiment with 1 round of measurements, we prepare each of the four dual-rail basis states. Using the results of the 2 rounds of measurements and our decoding strategy, we assign one of the four states {'00', '01', '10', '11'}, or the ambiguous outcome 'A' in the case where the two measurement outcomes disagree. Results of preparing the two logical state $|01\rangle$ and $|10\rangle$ are shown in the left two panels; results of intentionally preparing the leakage states $|00\rangle$ and $|11\rangle$ are shown in the right two panels. The green horizontal lines simulation results modeling the SPAM experiment with two-rounds of measurements. For each state, we repeat the experiment a total of 100, 000 times. The height of the each bar and center of the black line correspond to the mean of the data and error bars represent the standard error, showing $\pm 1\sigma$.

https://doi.org/10.1038/s41567-024-02539-4

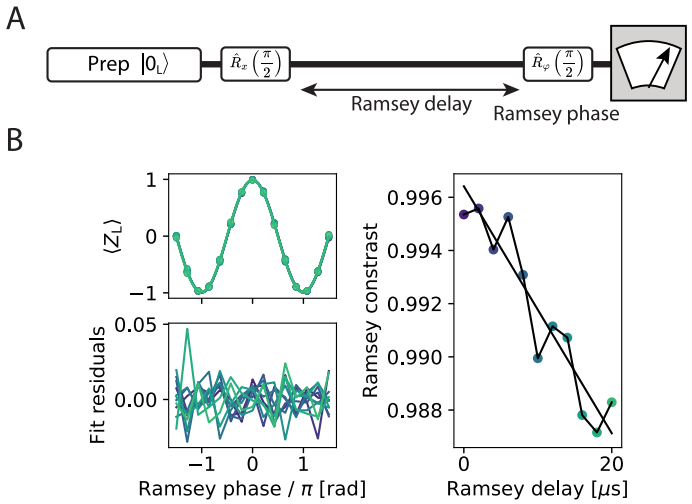

Extended Data Fig. 3 | Short-time Ramsey experiment analysis. (A) For these experiments, we perform a modified version of the Ramsey experiment described in the Main Text. Here we sweep both the Ramsey delay as well as the phase of the second $\pi/2$ pulse. (B) Top left: Logical results showing Ramsey oscillations for each delay out to 20 μs. The markers correspond to experimental results while the lines correspond to the fit. Bottom left: Fit residuals. Right: Extracted Ramsey contrast (valued between 0 and 1) as a function of Ramsey delay. Each marker corresponds to a different delay, color-coded to the data in the left column. Straight black line is a linear fit to the data.